PHYSICAL REVIEW C **83**, 044327 (2011)

# Isoscalar giant resonances in $^{48}$Ca

Y.-W. Lui, D. H. Youngblood, S. Shlomo, X. Chen,* Y. Tokimoto,† Krishichayan, M. Anders, and J. Button
*Cyclotron Institute, Texas A&M University, College Station, Texas 77843, USA*
(Received 14 February 2011; published 29 April 2011)

The giant resonance region from 9.5 MeV $< E_x <$ 40 MeV in $^{48}$Ca has been studied with inelastic scattering of 240-MeV $\alpha$ particles at small angles, including 0°. $95^{+11}_{-15}$% of $E0$ energy-weighted sum rule (EWSR), $83^{+10}_{-16}$% of $E2$ EWSR, and 137 ± 20% of $E1$ EWSR were located below $E_x = 40$ MeV. A comparison of the experimental data with calculated results for the isoscalar giant monopole resonance, obtained within the mean-field-based random-phase approximation, is also given.

DOI: 10.1103/PhysRevC.83.044327 PACS number(s): 24.30.Cz, 25.55.Ci, 27.40.+z, 21.60.Jz

## I. INTRODUCTION

The location of the isoscalar giant monopole resonance (ISGMR) is important because it can be directly related to the incompressibility coefficient of nuclear matter (NM) [1–3], an important ingredient in the equation of state (EOS) of NM. Systematic studies of the ISGMR energy $E_0$ in various nuclei lead to the value of $K_{\rm NM} = 231 \pm 5$ MeV [4] for the incompressibility coefficient of symmetric NM. This property of the ISGMR and the variation of the incompressibility coefficient with neutron number can also be used to extract the asymmetry coefficient $K_{\rm sym}$ in the EOS of asymmetric NM [5]. In the analysis of experimental data on $E_0$ it is common to employ two approaches: (i) Adopting a semiclassical model to relate $E_0$ to an incompressibility coefficient $K_A$ of the nucleus and (ii) carry out a Leptodermous ($A^{-1/3}$) expansion of $K_A$, similar to a mass formula, to parametrize $K_A$ into volume, surface, symmetry, and Coulomb terms [6,7], and (ii) carrying out microscopic calculations of the strength function $S(E)$ of the ISGMR, within a fully self consistent mean-field-based random-phase approximation (RPA), with specific interactions (see the review in Ref. [8]) and comparing with the experimental data. The values of $K_{\rm NM}$ and $K_{\rm sym}$, are then deduced from the interaction that best reproduced the experimental data.

In an early analysis of the experimental data on the ISGMR [7,9,10], the Leptodermous expansion of $K_A$ was used to determine the volume, surface, symmetry, and Coulomb coefficients. However, the limitations of such an analysis were pointed out in Refs. [2,7,11,12]. In particular, Shlomo and Youngblood showed that this type of analysis could not provide a unique solution, even including all available world data as of that time [7].

In recent years, studies of the isotope dependence and the extraction of the symmetry term $K_{\rm sym}$ have been mostly concentrated in heavy nuclei [13–15], especially in Sn isotopes where the neutron excess ratio $(N-Z)/A$ value changes from 0.107 in $^{112}$Sn to 0.194 in $^{124}$Sn. This gives a relative large deviation in the isotope dependence. However, in the calcium isotopes, $(N-Z)/A$ is 0 in $^{40}$Ca and 0.167 in $^{48}$Ca, a much larger variation than in the Sn isotopes, even though the neutron excess in $^{48}$Ca is not as large as in $^{124}$Sn. Thus a study of $^{40-48}$Ca might provide a more precise determination of the symmetry coefficient $K_{\rm sym}$. Strauch *et al.* studied giant resonances (GRs) in $^{48}$Ca [16] using inelastic scattering of electrons in coincidence with neutron decay. They extracted a strength function representing the combined isoscalar giant monopole and giant quadrupole resonance strengths as well as the strength function for the isovector giant dipole resonance. Due to similarity of the form factors in electron scattering between the ISGMR and isoscalar giant quadrupole resonance (ISGQR), they could not separate them.

We have previously reported ISGMR strength in $^{40}$Ca [17–19] and here we report a study of $^{48}$Ca with small-angle inelastic $\alpha$ scattering to obtain GR strength distributions. We also compare our experimental results with theoretical calculations of Refs. [20] and [21] and fully self-consistent Hartree-Fock-based RPA calculations [22] with commonly used Skyrme-type interactions, using the method of Refs. [23] and [24], and emphasize, in particular, the importance of self-consistency.

## II. EXPERIMENTAL TECHNIQUE AND DATA ANALYSIS

The experimental technique has been described thoroughly in Refs. [18,19,25] and is summarized briefly below. Beams of 240-MeV $\alpha$ particles from the Texas A&M University K500 superconducting cyclotron bombarded self-supporting $^{48}$Ca foils 4.4 mg/cm$^2$ thick enriched to more than 95% in $^{48}$Ca, located in the center of the target chamber of the multipole-dipole-multipole spectrometer. The horizontal acceptance of the spectrometer was 4° and the vertical acceptance was set at ±2°. Ray tracing was used to reconstruct the scattering angle. The out-of-plane scattering angle was not measured. A position resolution of ∼0.9 mm and scattering angle resolution of ∼0.09° were obtained. The target thickness was verified by measuring the energy loss of the 240-MeV $\alpha$ beam at 0°. Cross sections were obtained from the charge collected, target thickness, dead time, and known solid angle. The cumulative uncertainties in the above parameters result in an approximately ±10% uncertainty in absolute cross sections. $^{24}$Mg spectra were taken before and after each run, and the

*Present address: Department of Chemistry, Washington University at St. Louis, St. Louis, MO 63130.
†Present address: Higashi-Korien-cho 12-9, Neyagawa-shi, Osaka, 572-0081 Japan.

 

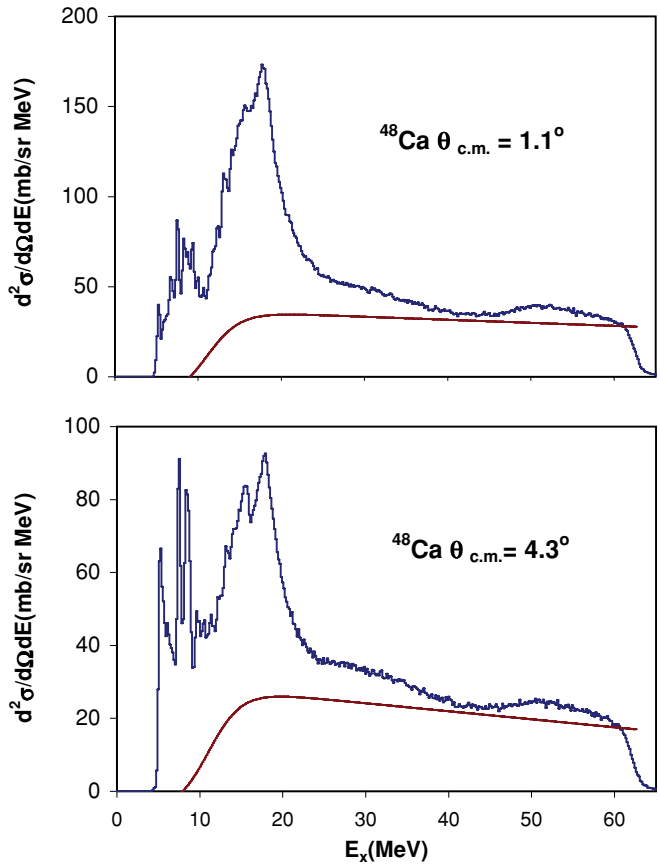


FIG. 1. Inelastic $\alpha$ spectra obtained for $^{48}$Ca. The solid lines show the continuum chosen for the analysis.

$13.85 \pm 0.02$ MeV $L = 0$ state [26] was used as a check on the calibration in the GR region.

GR data were taken with the spectrometer at 0.0° ($0.0° < \theta < 2.0°$), 4.0° ($2.0° < \theta < 6.0°$), and at 6.0° ($4.0° < \theta < 8.0°$). Sample spectra obtained for $^{48}$Ca are shown in Fig. 1. The GR peak can be seen extending up to $E_x \sim$ 40 MeV, but the peak-to-continuum ratio at higher excitation is much smaller than that in the main GR peak between 12 and 25 MeV. The spectrum was divided into a peak and a continuum, where the continuum was assumed to have the shape of a straight line in the high excitation region, joining onto a Fermi shape at low excitation to model particle threshold effects [25]. Samples of the continua used in the analysis are also shown in Fig. 1. Elastic scattering data and inelastic scattering data for low-lying states were taken over the range $2° \leqslant \theta_{\rm lab} \leqslant 32°$ to obtain optical parameters and test them by comparing $B(EL)$ values obtained for known states with adopted values.

## III. MULTIPOLE ANALYSIS

Single-folding density-dependent distorted-wave Born approximation (DWBA) calculations (as described in Refs. [18,25,27,28]) were carried out assuming a Fermi mass distribution for $^{48}$Ca having $c = 3.7231$ fm and $a = 0.523$ fm [29]. The transition densities, sum rules, and DWBA calculations were discussed thoroughly in Refs. [18,19,25] and, except for the ISGDR, the same expressions and techniques were used in this work. The transition density for inelastic $\alpha$-particle excitation of the ISGDR given by Harakeh and Dieperink [30] (and described in Refs. [18] and [25]) is for only one magnetic substate, so that the transition density given in Ref. [30] must be multiplied by $\sqrt{3}$ in the DWBA calculations.

TABLE I. Folding model parameters for $^{48}$Ca used in the DWBA calculations.

| $V$ (MeV) | $W$ (MeV) | $r_i$ | $A_i$ (fm) |
|---|---|---|---|
| 47.392 | 31.495 | 0.959 | 0.677 |

Folding model parameters for $^{48}$Ca were obtained by fitting data for elastic scattering of 240-MeV $\alpha$ particle from $^{48}$Ca over the range of center-of-mass (c.m.) angles 2.5°–40° and are listed in Table I. The fit obtained to the elastic scattering data with these parameters is shown in Fig. 2. DWBA calculations for the 3.832-MeV $2^+$ and 4.507-MeV $3^-$ states in $^{48}$Ca are shown superimposed on experimental data in Fig. 3. The extracted $B(EL)$ values for the $2^+$ and $3^-$ states are listed in Table II and compared to the values from other measurements [31–36]. The $B(E2)$ value for the 3.832-MeV $2^+$ state is consistent with the recent measurement using $^6$Li inelastic scattering [31] and is within the errors of the adopted value [32]. The $B(E3)$ value obtained for the 4.507-MeV $3^-$ state is lower than the adopted value [33] and is just outside the combined $1\sigma$ errors. The adopted value is from the measurement of inelastic scattering of polarized protons at 500 MeV, however, the value we obtain is in good agreement with three other measurements [31–36].

The multipole components of the GR peak were obtained [18,19,25] by dividing the peak into multiple regions (bins) by excitation energy and then comparing the angular distributions obtained for each of these bins to DWBA calculations. The uncertainty from the multipole fits was determined for each multipole by incrementing (or decrementing) that strength,

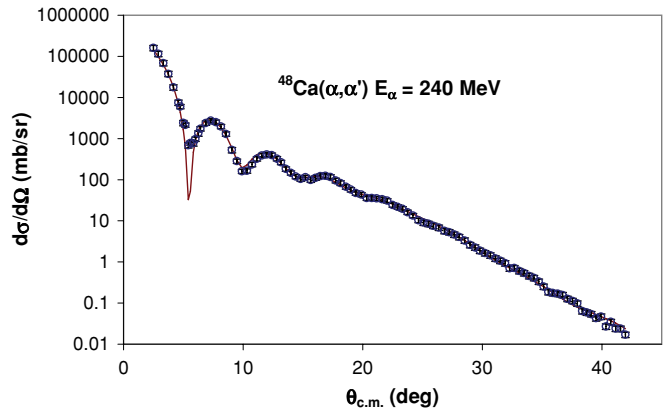


FIG. 2. (Color online) Angular distribution of the differential cross section for elastic scattering for 240-MeV $\alpha$ particles from $^{48}$Ca plotted vs c.m. angle. The error bars include uncertainty from statistical as well as systematic error. The solid line shows an optical model calculation with the parameters listed in Table I.

TABLE II. $B(EL)$ values for $2^+$ and $3^-$ states of $^{48}$Ca obtained in present work and from other references.

| | $E_x = 3.832$ MeV, $J^\pi = 2^+$ $B(E2)$ $(e^2b^2)$ | $E_x = 4.507$ MeV, $J^\pi = 3^-$ $B(E3)$ $(e^2b^3)$ |
|---|---|---|
| Present work | $0.0140 \pm 0.0015$ | $0.0054 \pm 0.0008$ |
| 240 Mev $^6$Li [31] | $0.0116 \pm 0.0012$ | $0.0075 \pm 0.0008$ |
| Adopted value | $0.0095 \pm 0.0032$ [32] | $0.0083 \pm 0.0020$ [33] |
| 25–40 MeV $p$ [34] | | 0.0054 |
| 800 MeV $p$ [35] | | 0.0063 |
| 65 MeV $p$ [36] | | 0.0048 |

then adjusting the strengths of the multipoles to minimize total $\chi^2$. This continued until the new $\chi^2$ was one unit larger than the total $\chi^2$ obtained for the best fit.

A sample of the angular distributions obtained for the GR peak and the continuum are shown in Fig. 4. Fits to the angular distributions were carried out with a sum of isoscalar $0^+$, $1^-$, $2^+$, $3^-$, and $4^+$ strengths. The isovector giant dipole resonance

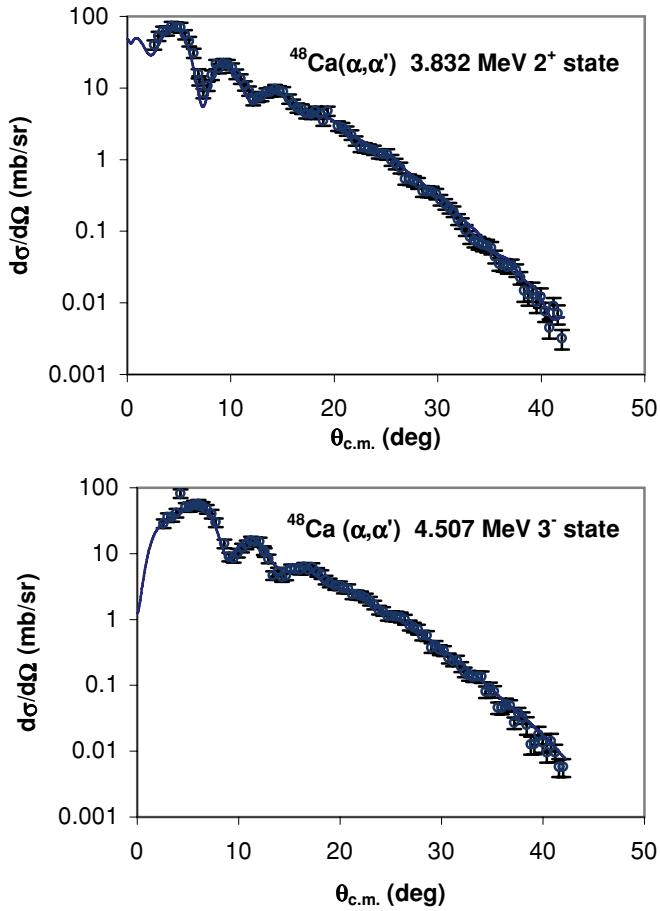


FIG. 3. (Color online) (Top) Angular distribution of the differential cross section for inelastic $\alpha$ scattering to the 3.832-MeV $2^+$ state in $^{48}$Ca. The solid line is the calculated inelastic scattering cross section for $B(E2) = 0.014e^2b^2$. (Bottom) Angular distribution of the differential cross section for inelastic $\alpha$ scattering to the 4.507-MeV $3^-$ state in $^{48}$Ca. The solid line shows an $L = 3$ DWBA calculation for $B(E3) = 0.0054e^2b^3$.

contributions were calculated from $^{40}$Ca parameters [37] by shifting the energy assuming an $A^{-1/3}$ dependence and were held fixed in the fits. Sample fits obtained, along with the individual components of the fits, are shown superimposed on the data in Fig. 4. The continuum distributions are similar over the entire energy range, whereas the angular distributions of the cross sections for the peak change as the contributions of different multipoles dominate in different energy regions.

Several analyses were carried out to assess the effects of different choices of the continuum on the resulting multipole distribution, as described in Ref. [38], where the continuum was systematically varied and the data were reanalyzed. The strength distributions obtained from these analyses using different choices of continuum and from those obtained with the continua shown in Fig. 1 were then averaged, and errors were calculated by adding the errors obtained from the multipole fits in quadrature to the standard deviations between the analyses with different continua.

The isoscalar $E0$, $E1$, $E2$, and $E3 + E4$ distributions obtained for the GR peak are shown in Fig. 5, and the energy moments and sum-rule strengths obtained are summarized in Table III. A single Gaussian was fit to the $E2$ strength distribution and two Gaussians were fit to the $E1$ distribution. These Gaussians are shown in Fig. 5 and the parameters obtained are listed in Table III. The $E0$, $E1$, $E2$, and $E3 + E4$ strength distributions obtained from fits to the continuum are shown in Fig. 6.

## IV. DESCRIPTION OF MICROSCOPIC CALCULATIONS

The microscopic mean-field-based RPA provides a good description of collective states in nuclei [1,8]. It is common to calculate the RPA states $|n\rangle$ with the corresponding energies $E_n$, and obtain the strength function

$$S(E) = \Sigma_n |\langle 0|F|n\rangle|^2 \delta(E - E_n)$$

for a certain single-particle scattering operator $F = \Sigma f(i)$, and then determine the energy moments

$$m_k = \int E^k S(E)\, dE.$$

The constrained energy $E_{\rm con}$, centroid energy $E_{\rm cen}$, and the scaling energy $E_s$ of the resonance are then obtained from

$$E_{\rm con} = (m_1/m_{-1})^{1/2}, \quad E_{\rm cen} = m_1/m_0, \quad E_s = (m_3/m_1)^{1/2}.$$

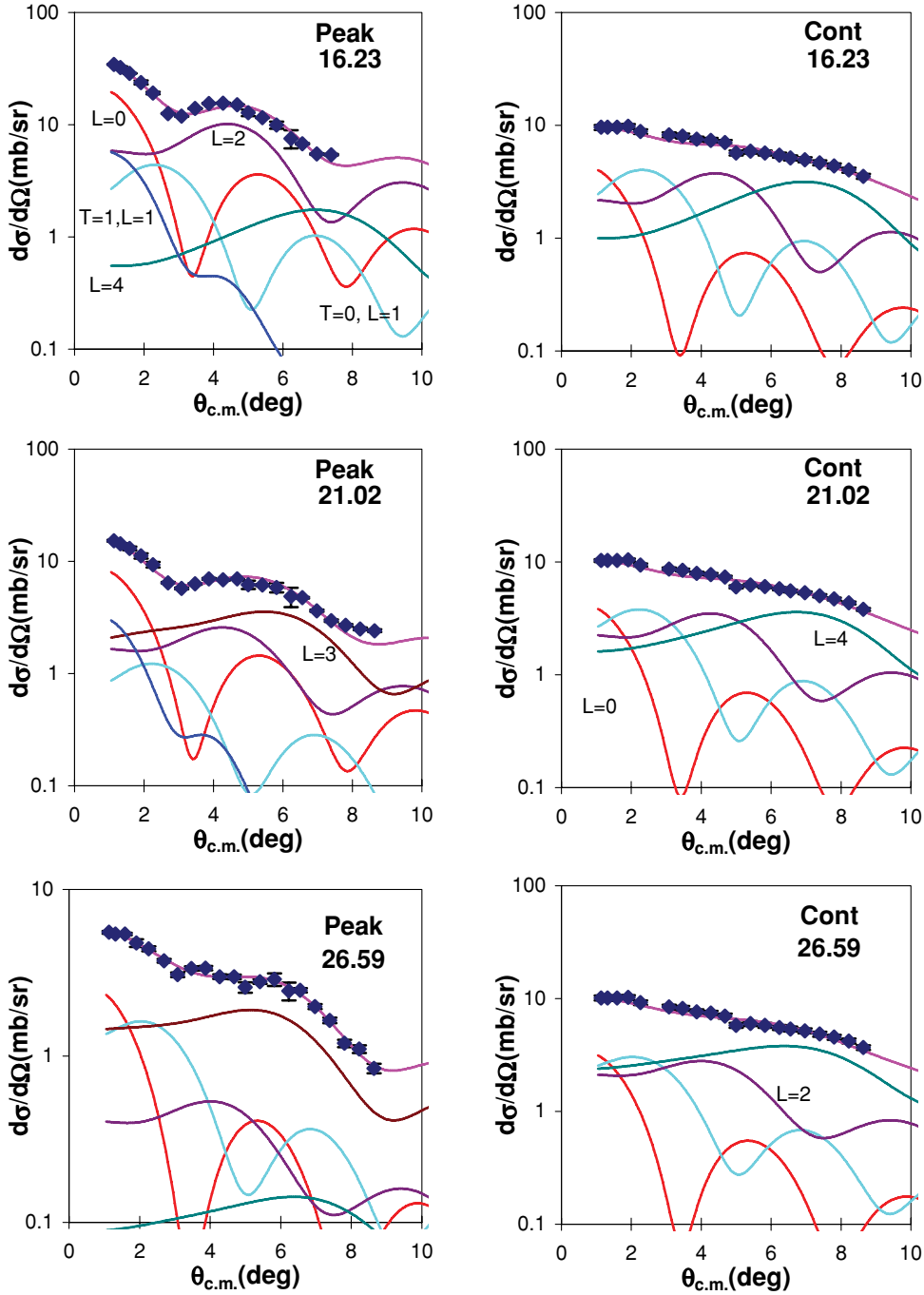


FIG. 4. (Color online) The angular distributions of the $^{48}$Ca cross section for three energy bins of the GR peak and the continuum. The excitation energy in MeV of the center of the bin is shown. The lines through the data points indicated the multipole fits. Contributions of each multipole are shown.

The energy moment $m_1$ can also be calculated using the Hartree-Fock (HF) ground-state wave function, leading to an energy-weighted sum rule (EWSR). In a fully self-consistent mean-field calculation of the response function, one adopts an effective two-nucleon interaction $V$, usually fitted to ground-state properties of nuclei, and determines the mean field. Then, the RPA calculation is carried out with all the components of the two-body interaction using a large configuration space. In this sense, the calculations are fully self-consistent. Employing the numerical approach of [23,24], we have carried out fully self-consistent HF-based RPA calculations of the ISGMR strength functions, for the scattering operator $f = r^2 Y_{00}$, for $^{40}$Ca and for $^{48}$Ca, using various Skyrme-type effective interactions; see Ref. [22] for details.

Hamamoto *et al.* [20], using the Green's function method [39] and various Skyrme-type interactions, carried out HF-based continuum RPA (CRPA) calculations of the ISGMR strength distributions in a number of Ca isotopes from $A = 34$

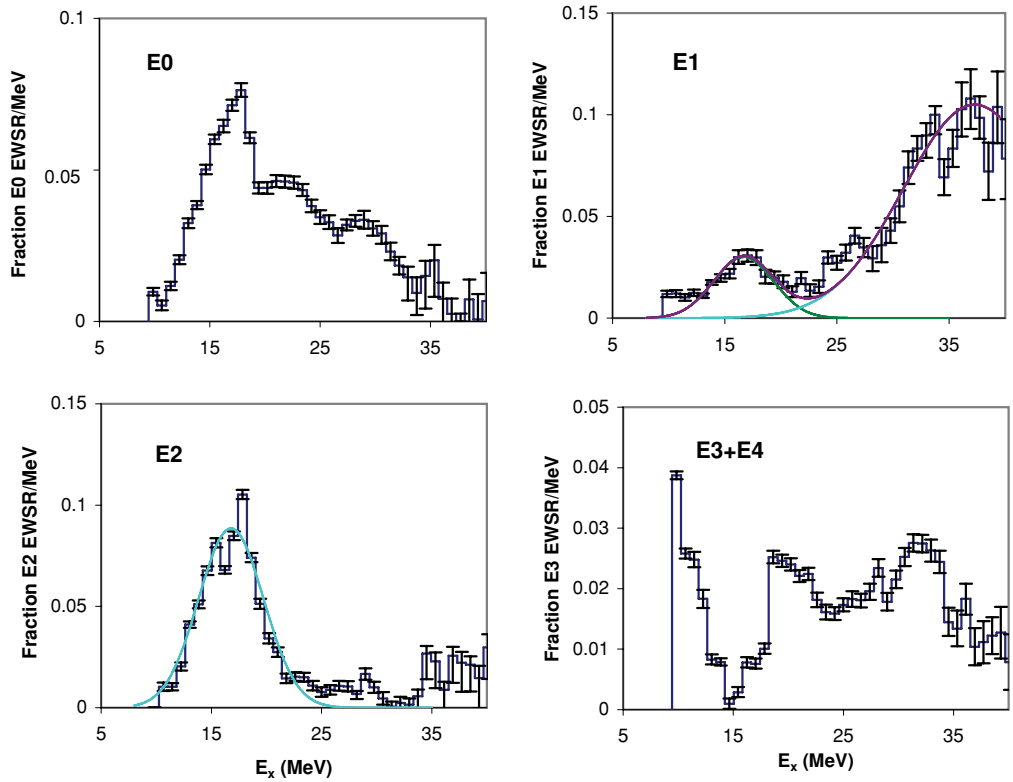


FIG. 5. (Color online) Isoscalar strength distributions obtained for $^{48}$Ca are shown by the histograms. Error bars represent the uncertainty from the fitting of the angular distributions and different choices of the continuum, as described in the text. Gaussian fits are shown as smooth lines. The vertical scale on the $E3 + E4$ distribution is in terms of the $E3$ EWSR only.

to $A = 60$. Although the important effects of the continuum (due to particle decay) were taken into account, the RPA calculations were not fully self-consistent due to the neglect of the particle-hole, spin-orbit, and Coulomb interactions. Kamerdzhiev *et al.* [21] have carried out microscopic calculations in CRPA including one particle-one hole ($1p1h$) coupled to phonon configurations for several nuclei including $^{48}$Ca. Unfortunately, Kamerdzhiev's calculations were done with effective interactions (Migdal-type interactions) which are unrelated to the adopted mean fields (Wood-Saxon potentials) and therefore cannot be used to determine the nuclear matter incompressibility coefficient. In the next section we will compare our experimental data with results of microscopic RPA calculations.

TABLE III. Parameters obtained for isoscalar multipoles in $^{48}$Ca.

| | Moments | | | |
|---|---|---|---|---|
| | $E0$ | $E1$ | $E2$ | $E3 + E4$ |
| $m_1$ (% EWSR) | $95^{+11}_{-15}$ | $137 \pm 20$ | $83^{+10}_{-16}$ | $55 \pm 13$ |
| $m_1/m_0$ (MeV) | $19.88^{+0.14}_{-0.18}$ | $27.30 \pm 1.30$ | $18.61^{+0.13}_{-0.34}$ | $20.90 \pm 0.14$ |
| rms width (MeV) | $6.68^{+0.31}_{-0.36}$ | $8.27 \pm 0.22$ | $7.96^{+0.26}_{-0.66}$ | $9.34 \pm 0.16$ |
| $(m_3/m_1)^{1/2}$ (MeV) | $22.64^{+0.27}_{-0.33}$ | $31.20 \pm 0.90$ | | |
| $(m_1/m_{-1})^{1/2}$ (MeV) | $19.04^{+0.11}_{-0.14}$ | $25.30 \pm 0.60$ | | |
| | | Gaussian fits | | |
| | | $E1$ peak 1 | $E1$ peak 2 | $E2$ |
| Centroids (MeV) | | $16.69^{+0.19}_{-0.13}$ | $37.28^{+0.71}_{-1.98}$ | $16.79^{+0.14}_{-0.12}$ |
| FWHM (MeV) | | $6.24^{+1.49}_{-0.11}$ | $14.95^{+3.49}_{-0.11}$ | $6.95^{+0.11}_{-0.35}$ |
| Frac. EWSR | | $0.20^{+0.12}_{-0.08}$ | $1.60^{+0.90}_{-0.50}$ | $0.65^{+0.09}_{-0.11}$ |

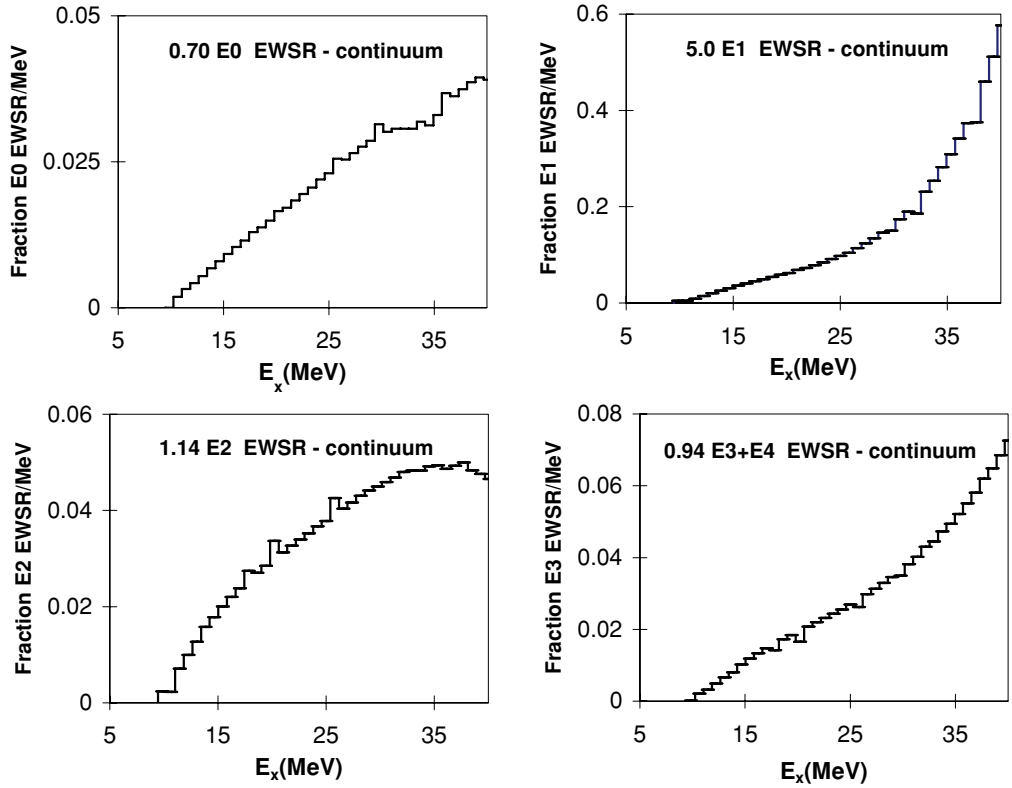


FIG. 6. $E0$, $E1$, $E2$, and $E3 + E4$ strength distributions obtained for $^{48}$Ca from the fit to the continuum. The total fraction of the EWSR is indicated for each. The vertical scale on the $E3 + E4$ distribution and the sum-rule fraction given are in terms of the $E3$ EWSR only.

## V. RESULTS AND DISCUSSION

$95^{+11}_{-15}$% of the $E0$ EWSR strength was located in $^{48}$Ca between 9.5 and 40 MeV centered $(m_1/m_0)$ at $19.88^{+0.14}_{-0.18}$ MeV. The shape of the strength distribution is asymmetric with a Gaussian-like shape in the low excitation region but with large tailing on the high excitation side extending to 40 MeV.

A total of $83^{+10}_{-16}$% of the $E2$ EWSR was found between 9.5 and 40 MeV. There is an almost Gaussian peak below 25 MeV contributing ∼65% of $E2$ EWSR and the rest is distributed roughly uniformly between 25 and 40 MeV. The combined $E0 + E2$ distributions from our work are compared to the electron scattering data [16] in Fig. 7. The shape of the distributions are in reasonable agreement between these two sets of data, but the strength extracted from the electron scattering data is lower.

Strength corresponding to $137 \pm 20$% of the ISGDR EWSR was identified between 9.5 and 40 MeV with a centroid at $27.3 \pm 1.3$ MeV. The distribution shows approximately two components. Gaussian fits to the distribution resulted in a small component at 16.7 MeV that exhausts 20% of EWSR and a much larger component at ∼37 MeV that exhausts 160% of EWSR. Much of this Gaussian second peak lies above 40 MeV where our analysis ended, so that the total $E1$ strength from the Gaussian fits is much larger than the value obtained by direct integration of the data. The strength of this second peak is extremely sensitive to the choice of continuum, as a large $E1$ component increasing rapidly with energy, is required to fit the angular distributions of the continuum as can be seen in Fig. 6, indicating that some processes responsible for the continuum have angular distributions similar to the $E1$ distribution. At $E_x = 40$ MeV the "$E1$" strength deduced from fits to the continuum is five times that in the peak (∼55% of the EWSR/MeV in continuum and ∼10% EWSR/MeV in the peak) so that a small change

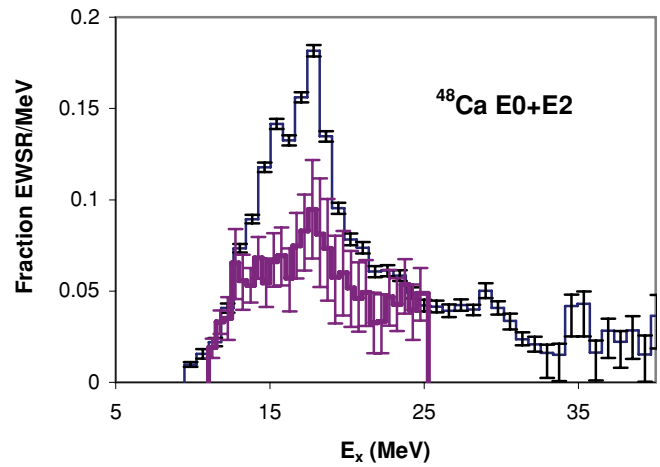


FIG. 7. (Color online) The $E0 + E2$ strength distribution obtained in this work for $^{48}$Ca is shown in the histogram with thin lines. The darker histogram is the $E0 + E2$ strength distribution obtained from inelastic electron scattering [16]. The vertical scale indicates the fraction of the $E0 + E2$ sum rule observed.

in the continuum would have a large effect on the strength attributed to $E1$ in the peak. The total $E1$ strength obtained from fits to the continuum corresponds to five times the $E1$ EWSR. A similar result has been seen in a number of other nuclei [38,40,41]. Therefore, small changes in assumptions about the continuum will drastically affect the $E1$ strength obtained for the GR peak, particularly at high excitation energy, leading to large uncertainties in the $E1$ distribution.

Due to the limited angular range of the data, $E3$ and $E4$ cannot reliably be separated from each other or from higher multipoles. The distribution shown in Fig. 5 has three regions of enhanced strength at ∼10, 20, and 33 MeV. In nearby nuclei ($^{46,48}$Ti [40], $^{56}$Fe,$^{58,60}$Ni [38]) the $E3$ distributions have a peak at low energy (∼10 MeV) and a broad distribution of strength extending from 15 MeV up to the highest excitation studied (∼35–40 MeV), though in $^{48}$Ti the $E3$ strength over this region has an almost Gaussian (but very broad) shape. In $^{24}$Mg and $^{28}$Si [42–44] the $E3$ strength observed was small and highly fragmented. In $^{40}$Ca, $E3$ and higher multipoles could not be separated, and the resulting distributions were not reported [18]. The strength seen in $^{48}$Ca below $E_x = 15$ MeV is similar to that seen in the $E3$ distributions in nearby nuclei and is most likely from the low-energy octupole resonance, but the source of the structure seen above $E_x = 15$ MeV in $^{48}$Ca is not known.

In general, the shape of the strength distributions in $^{48}$Ca are quite different from those for $^{40}$Ca [18], and they show less fine structure than in $^{40}$Ca. They are also quite different from the strength distributions in $^{46,48}$Ti [40], which are more Gaussian-like. The distributions in $^{48}$Ca are more similar to those in $^{58}$Ni [38]. The centroid ($m_1/m_0$) energies of the ISGMR obtained over the region $E_x = 9.5$ MeV to $E_x =$ 40 MeV for nuclei between mass 24 and mass 60 are plotted in Fig. 8. While the general trend is down with increasing $A$ and roughly going as $36/A^{1/6}$, $^{48}$Ca and $^{58}$Ni stand out as exceptions, both having considerably higher energies than some lighter nuclei. In particular, the $^{48}$Ca centroid is 0.7 MeV higher than that for $^{40}$Ca, and if the data between 5.4 and 9.5 MeV for $^{40}$Ca is included [17], this increases to 1.5 MeV. Fujita *et al.* [36], using inelastic proton scattering of 65 MeV protons, measured numerous states between 3.832 and 13.493 MeV in $^{48}$Ca and assigned $J^\pi$ values to most of them. Only two $0^+$ states were seen below our energy threshold, at 4.284 and 5.461 MeV, exhausting 0.13% and 0.34% of the $E0$ EWSR, which would lower the ISGMR centroid for $^{48}$Ca by 80 keV. This suggests that including the strength below 9.5 MeV, the $^{48}$Ca centroid is ∼1.4 MeV higher than $^{40}$Ca, however, since some strength may have been missed in the proton scattering (there are several peaks below 9.5 MeV in the Fujita *et al.* data for which no assignments could be made), in our discussions below we will use centroids obtained with data above $E_x =$ 9.5 MeV for both $^{48}$Ca and $^{40}$Ca.

While the continuum is likely from a number of (mostly) complex reactions, the strength contributions obtained by fitting the continuum angular distributions with a sum of $E0$–$E4$ multipole distributions provides an indication of the sensitivity of the strength distributions obtained for the peaks to the continuum chosen. They (Fig. 6) show few distinct features except that the strengths increase with increasing excitation energy, which are quite different from the strength distributions obtained from the peak. At all energies the $E1$ strength obtained from the continuum exceeds the sum of the other multipoles and the total represents five times the sum-rule strength. From this, one can conclude that the total $E1$ strength

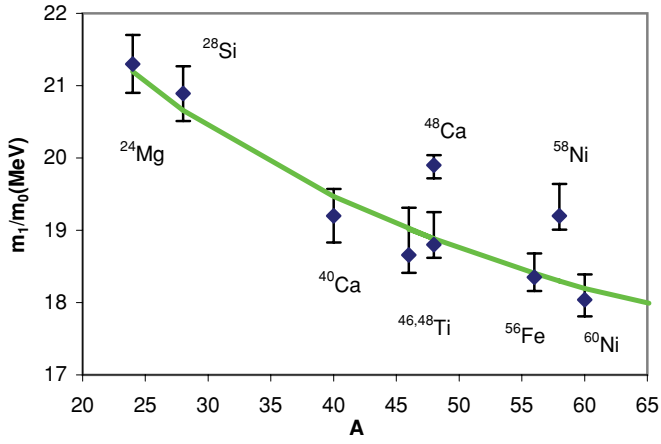


FIG. 8. (Color online) Centroid energies ($m_1/m_0$) for the ISGMR calculated over the energy range $E_x = 9.5 - 40$ MeV for nine nuclei are plotted as a function of $A$. (See text for the references). A line representing $36/A^{1/6}$ shows the trend.

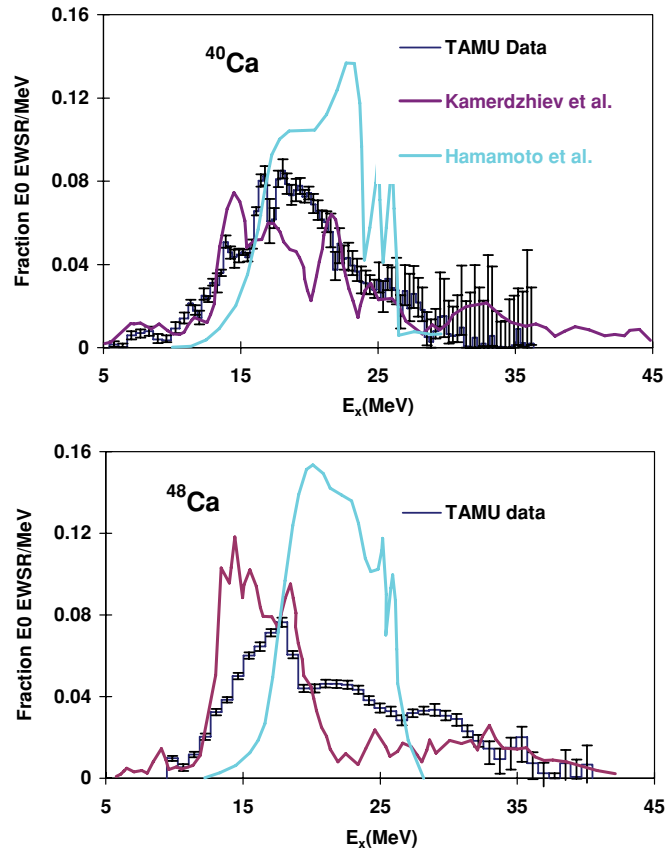


FIG. 9. (Color online) Experimental $E0$ strength distributions in $^{40,48}$Ca (histogram) are compared to calculations from Hamamoto *et al.* [20] (gray line) and Kamerdzhiev *et al.* [21] (black line).

in the peak will be quite sensitive to the continuum chosen, whereas the other multipoles will be affected much less by the choice of the continuum.

The $E0$ strength distributions obtained by Hamamoto *et al.* [20] and by Kamerdzhiev *et al.* [21] for $^{40}$Ca and $^{48}$Ca are compared to our measured distributions in Fig. 9. In Refs. [17] and [18] calculations of cross sections for excitation of the $E0$ strength in $^{40}$Ca at $\theta_{\mathrm{c.m.}} = 1.08^{\circ}$ by Kamerdzhiev *et al.* showed excellent agreement with the experimental data. The $E0$ strength distributions shown in Fig. 9 for $^{40}$Ca are not in as good agreement, suggesting that the microscopic transition densities used by Kamerdzhiev *et al.* varied somewhat over the energy range of the data, whereas our analysis assumed a collective transition density which does not change. Kamerdzhiev *et al.*'s calculated distribution for $^{48}$Ca peaks at lower excitation than the data, and while there is strength predicted at higher excitation, it is considerably weaker than in the data. Hamammoto *et al.*'s calculations show an ∼10-MeV-wide bump (with some fine structure) in both $^{40}$Ca and $^{48}$Ca, with little resemblance to the shape of the data.

The strength distributions obtained from our fully self-consistent HF-based RPA calculations obtained using the Skyrme-type SGII [45], SKM* [46], KDE0 [47], and SK255 [48] interactions are compared to experimental data in Fig. 10. A 3-MeV Lorentzian smearing function has been applied to the predicted distributions to aid visual comparison to the data.

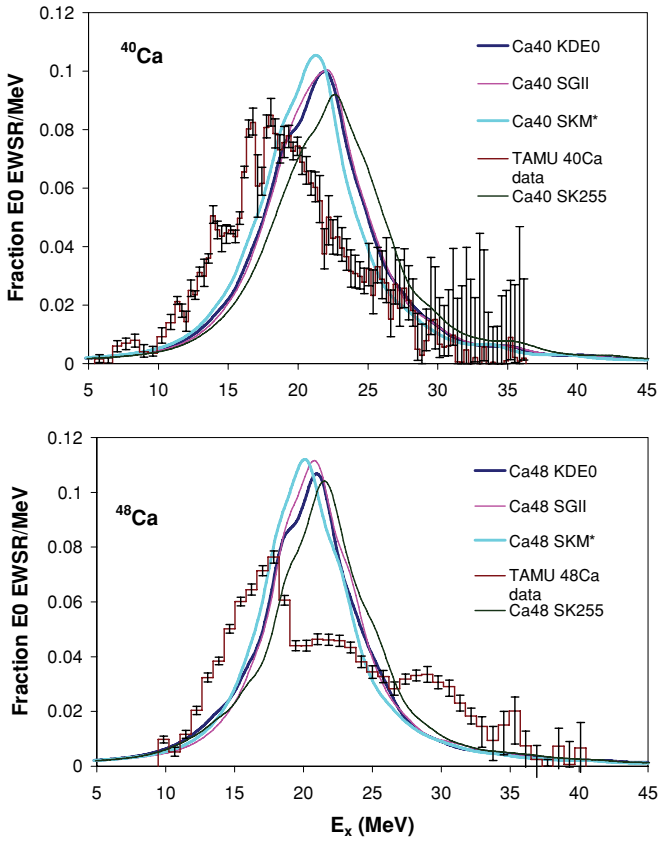


FIG. 10. (Color online) HF-RPA calculations with four interactions after application of a 3-MeV Lorentzian smearing function, are compared to experimental $E0$ strength distributions in $^{40,48}$Ca (histogram).

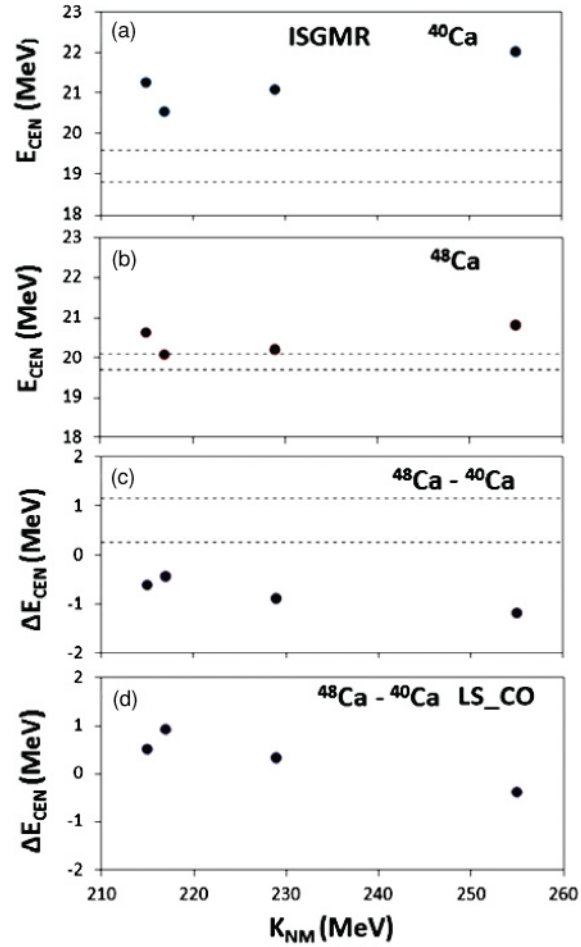


FIG. 11. Comparison of experimental data of the centroid energies $E_{\mathrm{cen}}$ of $^{40}$Ca (a), $^{48}$Ca (b), and the energy difference between $^{48}$Ca and $^{40}$Ca (c), shown as the regions between the dashed lines, with the results of fully self-consistent HF-based RPA calculations (full circles), using the SGII [45], SKM* [46], KDE0 [47], and SK255 [48] Skyrme-type interactions having nuclear matter incompressibility coefficients $K_{\mathrm{NM}} = 215$, 217, 230, and 255 MeV, respectively. The results obtained with violation of self-consistency by neglecting the Coulomb and the spin-orbit interactions in the RPA calculations are shown in (d). The energies shown were calculated over the experimental excitation energy range of 9.5–40 MeV.

The shapes of the calculated distributions for $^{40}$Ca are in fair agreement with the data, but the calculated distributions peak 2–4 MeV higher than the data. For $^{48}$Ca, the data also peak several MeV below the calculations, and the calculations do not reproduce the large tailing seen at higher excitation.

In Table IV we compare the measured energies in $^{40,48}$Ca to those obtained in the calculations of Refs. [20] and [21] and with fully self-consistent HF-based RPA obtained [22] with various Skyrme-type SGII [45], SKM* [46], KDE0 [47], and SK255 [48] interactions. The selected Skyrme interactions are associated with a wide range of NM incompressibility coefficients $K = 215$–$255$ MeV and a wide range of NM symmetry energy coefficients $J = 27$–$37$ MeV. The values from Refs. [20] and [21] are calculated over the full energy range shown in the references, while those from our calculations are

TABLE IV. Experimental results for ISGMR energies in $^{40}$Ca [18] and $^{48}$Ca (present work) are compared with theoretical predictions. The results of fully self-consistent calculations [22] with Skyrme interactions SGII, SKM*, KDE0, and SK255, which are associated with the nuclear matter incompressibility coefficients $K_{\rm NM} = 215$, 217, 230, and 255 MeV, respectively, are shown using the experimental excitation range of $E = 9.5$–40 MeV (first line) and the extended range $E = 0$–60 MeV (second line).

| | $^{40}$Ca | | | $^{48}$Ca | | | $\Delta E_{\rm cen}$ |
|---|---|---|---|---|---|---|---|
| | $(\frac{m_1}{m_{-1}})^{1/2}$ (MeV) | $\frac{m_1}{m_0}$ (MeV) | $(\frac{m_3}{m_1})^{1/2}$ (MeV) | $(\frac{m_1}{m_{-1}})^{1/2}$ (MeV) | $\frac{m_1}{m_0}$ (MeV) | $(\frac{m_3}{m_1})^{1/2}$ (MeV) | (MeV) |
| Experiment | $18.3 \pm 0.3$ | $19.2 \pm 0.4$ | $20.6 \pm 0.4$ | $19.0 \pm 0.1$ | $19.9 \pm 0.2$ | $22.6 \pm 0.3$ | 0.7 |
| Hamamoto *et al.* [20] | 20.5 | 20.8 | 22.0 | 21.4 | 21.6 | 22.6 | 0.8 |
| Kamerdzhiev *et al.* [21] | 16.9 | 18.5 | 23.2 | 16.8 | 17.7 | 21.3 | −0.8 |
| SGII [45] | 21.0 | 21.3 | 22.0 | 20.4 | 20.6 | 21.2 | −0.7 |
| | 21.1 | 21.4 | 22.7 | 20.5 | 20.7 | 21.6 | −0.7 |
| SKM* [46] | 20.3 | 20.5 | 21.3 | 19.9 | 20.1 | 20.7 | −0.4 |
| | 20.4 | 20.7 | 22.0 | 19.9 | 20.2 | 21.1 | −0.5 |
| KDE0 [47] | 20.8 | 21.1 | 21.9 | 19.9 | 20.2 | 21.0 | −0.9 |
| | 20.9 | 21.3 | 22.7 | 20.0 | 20.3 | 21.5 | −1.0 |
| SK255 [48] | 21.7 | 22.0 | 22.9 | 20.5 | 20.8 | 21.7 | −1.2 |
| | 21.8 | 22.2 | 23.7 | 20.6 | 21.0 | 22.3 | −1.2 |

shown both for the experimental energy range (9.5–40 MeV) and over the full range of the calculations (0–60 MeV). In Fig. 11 we show the centroid energies as a function of $K_{\rm NM}$. As can be seen in Fig. 11(b), for $^{48}$Ca, the centroid obtained with SKM* is in agreement with the data, while that for KDE0 is slightly outside the errors and those for the other two interactions are a few hundred keV outside the errors. For $^{40}$Ca [Fig. 11(a)] the centroid obtained with SKM* is high and ∼600 keV outside the errors, while those for the other interactions are yet higher and over a MeV outside the errors.

Whereas in the Sn isotopes the ISGMR energy decreases with increasing mass, the measured $^{48}$Ca centroid energy is higher than that for $^{40}$Ca. The measured centroid energy given in Table IV for $^{40}$Ca is 0.7 MeV *below* that of $^{48}$Ca. It was obtained over the energy range we measured for $^{48}$Ca ($E_x = 9.5 - 40$ MeV) using the experimental results of Ref. [18] for $^{40}$Ca. Taking into account the known excitation strength below 10 MeV in $^{40}$Ca [17], and in $^{48}$Ca [36], the centroid energy for $^{48}$Ca would be higher than that of $^{40}$Ca by ∼1.4 MeV, enhancing this difference.

The energies of the ISGMR in $^{48}$Ca obtained in our fully self-consistent calculations using various Skyrme-type interactions are all 0.7–1.2 MeV *below* those of $^{40}$Ca [Fig. 11(c)]. From Table IV it can be seen that when obtaining the centroids from the HF-RPA calculations, extending the range from that for the experimental data (9.5–40 MeV) to the full range of the calculations (0–60 MeV) changed the $^{48}$Ca-$^{40}$Ca energy difference by at most 100 keV.

Kamerdzhiev *et al.*'s calculations [21] give a difference −0.8 MeV (in the opposite direction of the data), and Hamamoto *et al.*'s calculation [20] with the SKM* [47] interaction gives an energy difference of +0.8 MeV (close to that of the experimental data). Unfortunately, Hamamoto *et al*'s. calculations are not fully self-consistent. The effects of self-consistency violation on transition densities and energies of GRs are discussed in Refs. [24,49–52]. In particular, it was shown by Sil *et al.* [24] that the effects of self-consistency violation associated with neglecting the particle-hole spin-orbit and Coulomb interactions in HF-based RPA calculations can shift GR energies by hundreds of keV. Calculations following the description in Sec. IV but neglecting the particle-hole spin-orbit and Columb interactions [22] give $^{48}$Ca energies higher relative to $^{40}$Ca than those that include these interactions by 0.4–1.2 MeV. Leaving out these interactions, the predicted ISGMR centroid energies [Fig. 11(d)] in $^{48}$Ca are higher than those in $^{40}$Ca by $\Delta E_{\rm cen} = 0.5$, 0.3, and 1.0 MeV for the SGII, KDE0, and SkM∗ interactions, and SK255 gives a $^{48}$Ca energy below $^{40}$Ca by 0.4 MeV.

## VI. CONCLUSION

Close to 100% of the isoscalar $E0$, $E1$, and $E2$ strengths have been located between 9.5 and 40 MeV in $^{48}$Ca. The angular distributions of the continuum are similar to those for $E1$ excitation, so the $E1$ strength distribution obtained for the GR peak is very sensitive to the choice of continuum. The $E0$ distribution is very asymmetric with a strong tail at higher excitation, more similar to $^{58}$Ni than $^{40}$Ca or $^{48}$Ti, and thus the centroid energy $(m_1/m_0)$ in $^{48}$Ca is higher than the $36/A^{1/6}$ trend for most nuclei between $^{24}$Mg and $^{60}$Ni. The experimental energy $(m_1/m_0)$ of the ISGMR in $^{48}$Ca is 0.7–1.4 MeV higher that in $^{40}$Ca, in approximate agreement with non-self-consistent calculations by Hamamoto *et al.*, but self-consistent microscopic calculations with SGII, KDE0, SKM*, and SK255 Skyrme interactions all predict a lower centroid in $^{48}$Ca than in $^{40}$Ca. On the other hand, the microscopic calculations do not reproduce the experimental strength distributions, particularly for $^{48}$Ca, and the predicted centroids are generally higher than experiment, so that nuclear structure issues not taken into account in the calculations may be a serious issue in these relatively light nuclei.

In summary, the ISGMR has been found at somewhat higher energy in $^{48}$Ca than in $^{40}$Ca, whereas self consistent

HF-RPA calculations predict a lower centroid energy in this neutron-rich Ca isotope. The calculations do not reproduce the strength distributions, and it would be interesting to extend them beyond the RPA to include coupling to more complex configurations. Also an analysis of the experimental data using microscopic transition densities in the DWBA calculations should be undertaken [53]. Experimentally it would be useful to use small-angle $\alpha$ scattering to look for $0^+$ strength in $^{48}$Ca below the $E_x = 9.5$ MeV lower limit of this experiment, which might lower the $^{48}$Ca centroid. Better knowledge of the continuum could reduce uncertainties, particularly at higher excitation where the ISGMR cross section is low, and the use of microscopic transition densities could also change the energy dependence of the extracted strength, which could affect centroid energies in both $^{40}$Ca and $^{48}$Ca.

## ACKNOWLEDGMENT

This work was supported in part by the US Department of Energy under Grant No. DE-FG02-93ER40773.

[1] A. Bohr and B. M. Mottelson, *Nuclear Structure II* (Benjamin, New York, 1975).
[2] J. P. Blaizot, Phys. Rep. **64**, 171 (1980).
[3] S. Stringari, Phys. Lett. B **108**, 232 (1982).
[4] D. H. Youngblood, H. L. Clark, and Y.-W. Lui, Phys. Rev. Lett. **82**, 691 (1999).
[5] J. Piekarewicz and M. Centelles, Phys. Rev. C **79**, 054311 (2009).
[6] J. Treiner, H. Krivine, O. Bohigas, and J. Martorell, Nucl. Phys. A **371**, 253 (1981).
[7] S. Shlomo and D. H. Youngblood, Phys. Rev. C **47**, 529 (1993), and references therein.
[8] S. Shlomo, V. M. Kolomietz, and G. Colo, Eur. Phys. J. A **30**, 23 (2006), and references therein.
[9] D. H. Youngblood, P. Bogucki, J. D. Bronson, U. Garg, Y.-W. Lui, and C. M. Rozsa, Phys. Rev. C **23**, 1997 (1981).
[10] M. M. Sharma, W. T. A. Borghols, S. Brandenburg, S. Crona, A. Van der Woude, and M. N. Harakeh, Phys. Rev. C **38**, 2562 (1988).
[11] J. M. Pearson, Phys. Lett. B **271**, 12 (1991).
[12] J. M. Pearson, N. Chamel, and S. Goriely, Phys. Rev. C **82**, 037301 (2010).
[13] Y.-W. Lui, D. H. Youngblood, Y. Tokimoto, H. L. Clark, and B. John, Phys. Rev. C **70**, 014307 (2004).
[14] Y.-W. Lui, D. H. Youngblood, Y. Tokimoto, H. L. Clark, and B. John, Phys. Rev. C **69**, 034611 (2004).
[15] T. Li *et al.*, Phys. Rev. C **81**, 034309 (2010).
[16] S. Strauch, P. von Neumann-Cosel, C. Rangacharyulu, A. Richter, G. Schrieder, K. Schweda, and J. Wambach, Phys. Rev. Lett. **85**, 2913 (2000).
[17] D. H. Youngblood, Y.-W. Lui, H. L. Clark, Y. Tokimoto, and B. John, Phys. Rev. C **68**, 057303 (2003).
[18] D. H. Youngblood, Y.-W. Lui, and H. L. Clark, Phys. Rev. C **63**, 067301 (2001).
[19] D. H. Youngblood, Y.-W. Lui, and H. L. Clark, Phys. Rev. C **55**, 2811 (1997).
[20] I. Hamamoto, H. Sagawa, and X. Z. Zhang, Phys. Rev. C **56**, 3121 (1997).
[21] S. Kamerdzhiev, J. Speth, and G. Tertchny, Eur. Phys. J. A **7**, 483 (2000); Phys. Rep. **393**, 1 (2004).
[22] M. Anders *et al.* (unpublished).
[23] P.-G. Reinhardt, Ann. Phys. (Leipzig) **1**, 632 (1992).
[24] T. Sil, S. Shlomo, B. K. Agrwal, and P.-G. Reinhard, Phys. Rev. C **73**, 034316 (2006).
[25] D. H. Youngblood, Y.-W. Lui, and H. L. Clark, Phys. Rev. C **65**, 034302 (2002).
[26] K. van der Borg, M. N. Harakeh, and A. van der Woude, Nucl. Phys. A **365**, 243 (1981).
[27] H. L. Clark, Y.-W. Lui, and D. H. Youngblood, Phys. Rev. C **57**, 2887 (1998).
[28] G. R. Satchler and D. T. Khoa, Phys. Rev. C **55**, 285 (1997).
[29] G. Fricke, C. Bernhardt, K. Heilig, E. B. Shera, and C. W. De Jager, At. Data Nucl. Data Tables **60** 177 (1995).
[30] M. N. Harakeh and A. E. L. Dieperink, Phys. Rev. C **23**, 2329 (1981).
[31] Krishichayan, X. Chen, Y.-W. Lui, J. Button, and D. H. Youngblood, Phys. Rev. C **81**, 044611 (2010).
[32] S. Raman, C. W. Nestor, and P. Tikkanen, At. Data Nucl. Data Tables **78**, 1 (2001).
[33] T. Kibedi and R. H. Spear, At. Data Nucl. Data Tables **80**, 35 (2002).
[34] C. R. Gruhn, T. Y. T. Kuo, C. J. Maggiore, and B. M. Preedom, Phys. Rev. C **6**, 944 (1972).
[35] G. S. Adams, Th. S. Bauer, G. Igo, G. Pauletta, C. A. Whitten Jr., A. Wriekat, G. W. Hoffmann, G. R. Smith, and M. Gazzaly, Phys. Rev. C **21**, 2485 (1980).
[36] Y. Fujita, M. Fujiwara, S. Morinobu, T. Yamazaki, T. Itahashi, H. Ikegami, and S. I. Hayakawa, Phys. Rev. C **37**, 45 (1988).
[37] Samuel S. Dietrich and Barry L. Berman, At. Data Nucl. Data Tables **38**, 199 (1988).
[38] Y.-W. Lui, D. H. Youngblood, H. L. Clark, Y. Tokimoto, and B. John, Phys. Rev. C **73**, 014314 (2006).
[39] S. Shlomo and G. F. Bertsch, Nucl. Phys. A **243**, 507 (1975).
[40] Y. Tokimoto, Y.-W. Lui, H. L. Clark, B. John, X. Chen, and D. H. Youngblood, Phys. Rev. C **74**, 044308 (2006).
[41] D. H. Youngblood, H. L. Clark, and Y.-W. Lui, Phys. Rev. Lett. **76**, 1429 (1996).
[42] D. H. Youngblood, Y.-W. Lui, X. F. Chen, and H. L. Clark, Phys. Rev. C **80**, 064318 (2009).
[43] D. H. Youngblood, Y.-W. Lui, and H. L. Clark, Phys. Rev. C **76**, 027304 (2007).
[44] X. Chen, Y.-W. Lui, H. L. Clark, Y. Tokimoto, and D. H. Youngblood, Phys. Rev. C **80**, 014312 (2009).
[45] Nguyen Van Giai and H. Sagawa, Phys. Lett. B **106**, 379 (1981).
[46] J. Bartel, P. Quentin, M. Brack, C. Guet, and H. B. Hakansson, Nucl. Phys. A **382**, 79 (1986).
[47] B. K. Argawal, S. Shlomo, and V. K. Au, Phys. Rev. C **72**, 014310 (2005).
[48] B. K. Argawal, S. Shlomo, and V. Kim Au, Phys. Rev. C **68**, 031304 (2003).
[49] S. A. Fayans, E. L. Trykov, and D. Zawischa, Nucl. Phys. A **568**, 523 (1994).

[50] M. L. Gorelik, S. Shlomo, and M. H. Urin, Phys. Rev. C **62**, 044301 (2000).
[51] S. Shlomo and A. I. Sanzhur, Phys. Rev. C **65**, 044310 (2002); S. Shlomo, Pramana J. Phys. **57**, 557 (2001).
[52] G. Colo, N. V. Giai, J. Meyer, K. Bennaceur, and P. Bonche, Phys. Rev. C **70**, 024307 (2004).
[53] A. Kolomiets, O. Pochivalov, and S. Shlomo, Phys. Rev. C **61**, 034312 (2000).